Thermo-metallo-mechanical based phase transformation modeling for high-speed milling of Ti–6Al–4V through stress-strain and temperature effects

Irfan Ullah [a], Esther Titilayo Akinlabi [b], Victor Songmene [a],*

[a] Department of Mechanical Engineering, École de Technologie Supérieure (ÉTS), 1100 Notre-Dame Street West, Montréal, QC, H3C 1K3, Canada
[b] Department of Mechanical and Construction Engineering, Northumbria University, Newcastle Upon Tyne, NE1 8ST, United Kingdom

ABSTRACT

The optimization of machining parameters, tool longevity, and surface quality in High-Speed Milling (HSM) of Ti–6Al–4V relies immensely on understanding the local phase transformation. This study endeavors to build a Finite Element (FE) model capable of forecasting phase alterations during the rapid thermal fluctuations intrinsic to Ti–6Al–4V machining. Dynamic phase transformation models were initially introduced to capture rapid heating and cooling phenomena. Using a user-defined subroutine, the phase transitions predictive models were integrated into the HSM simulation within Abaqus/Explicit. Simulation outcomes unveiled phase transitions primarily occurring within the serrated chip and at the tool-workpiece interface. Notably, during rapid heating, when the cutting speed increased to 350 m/min, the β-phase volume fraction surged from 7.5 to 96.38%. A similar trend was observed with feed rate adjustments (i.e., 0.15–0.25 mm/tooth), where β-phase increased from 7.5 to 67.84%. Rapid cooling facilitated the reversion of the transformed β-phase back into the α'-phase. Finally, some advanced characterization techniques were employed to validate the developed thermo-metallo-mechanical coupled FE model for phase transformation. The simulation results verified by the experimental data promotes a better understanding of phase alteration mechanisms and microstructural evolution in HSM of Ti–6Al–4V. The current research is also beneficial for crucial insights into optimizing the machining conditions and their impact on tool-material interactions and surface integrity.

1. Introduction

Ti–6Al–4V, a dual-phase alloy, has been broadly devoted in various sectors, including biomedical, aerospace, die, and mold, due to its enhanced mechanical strength and high corrosion resistance at elevated thermal conditions [1,2]. However, the machining of Ti–6Al–4V presents several challenges due to its low thermal conductivity, high chemical reactivity, and the tendency for serrated chip production [3]. These characteristics contribute to the appearance of complex behaviors during machining, such as increased temperatures, intense plastic deformation, alteration in grain structure, and phase transition. On the one hand, the heat and stresses triggered in the cutting deformation zones can lead to phase changes that have an unfavorable consequence on the surface integrity, which can cause the work hardening and lead to white layer formation. On the other hand, these thermo-mechanical loading histories have the potential to influence the stress state

through phenomena such as thermal softening and thermal strains [4]. Additionally, they can also impact the metallurgical conditions of material in accordance to the phase transformation kinetics.

Previous research has repeatedly mentioned the occurrence of phase transformation during the manufacturing of titanium and its alloys. However, it is difficult to characterize the phase transformation by standard methods, as the highly coupled behavior of thermal and mechanical loads and energy conversion in the HSM is a typically nonlinear problem. Numerous research studies have been undertaken to explore the occurrence of phase transformation of titanium in friction stir welding [5], hot forging [6], and laser sintering processes [7]. However, while machining, the prediction of phase transformation becomes more challenging as it simultaneously involves multi-faceted stress, high strain rates, and thermal loading history. In the late 90s, Bayoumi et al. [8] realized the non-diffusional phase transition occurrence within the Adiabatic Shear Band (ASB) of Ti–6Al–4V. However, contradictory

results (i.e., no phase transformation in the shear band) were presented by Puerta et al. [9]. By utilizing Transmission Electron Microscopy (TEM), Wan et al. [10] analyzed the existence of martensitic phase transition during the rapid cooling process. However, the authors could not detect any β-phase in their observations. The absence of the β-phase was attributed to the post-cooling experiments, a stage during which the β-phase had converted back into the α-phase. Similarly, Wang et al. discovered a gradual variation in the microstructures between the matrix and the center of ASB during the machining of 30CrNi3MoV, which may have undergone a martensitic phase change. Although substantial experimental work regarding the phase transformation of titanium and its alloys is available in the published literature. Nevertheless, most of the published research is related to conventional heat treatment. Unlike conventional methods, the phase transformation during the machining process is generally associated with mechanical load, severe plastic deformation, and rapid heating and quenching process. In addition, no systematic investigation has been conducted to investigate how machining factors explicitly impact the phase transition in Ti–6Al–4V.

Since predicting phase transition in mechanical machining is challenging to capture, the finite element (FE) model is becoming the most popular among researchers and industries for predicting phase transformation. Wang et al. [11] developed an FE model for predicting the phase alteration during machining of Ti–Al–4V and concluded that cutting speeds significantly influence the rapid heating and cooling process. Using cutting temperature as the determining factor, Zhang et al. [12] developed an FE model to predict phase changes in Ti–6Al–4V machining. Although the authors explored the phase transition behavior in machining deformation zones. However, their study relied on a steady-state phase transition assumption, which may inevitably lead to specific prediction errors. Ramesh et al. [13] developed a 2D FE model for predicting the white layer during orthogonal cutting of AISI52100 steel and concluded that the white layer is directly related to residual stress formation. Similarly, contemplating stress-strain effects, Li et al. [14] elaborated on the phase transformation in the hard cutting of H13 steel. They anticipated the austenite volume fraction in the chip back-surface. Like the cutting process, Bailey et al. [15] presented a three-dimensional FE model for predicting phase transformation during direct laser deposition. Considering various cooling stages during wire laser additive manufacturing of Ti–6Al–4V, Sun et al. [1] recently applied a density-based constitutional model for predicting phase transformation. They concluded that the increased temperature and decreased cooling rates significantly impact the formation process of α'-phase (with hexagonal structure). Taking Ni–Ti alloy as a research objective, Kaynak et al. [16] presented an FE model for phase transformation based on Helmholtz free energy. However, the authors only considered the layer subjected to twinning for model validation. Although few researchers have observed and verified phase transformation as a fundamental mechanism during machining with complex stress states, a well-established theoretical model for high-stress-strain-assisted transformation mechanisms is still lacking in predicting phase transformations. In addition, the existing research also indicates that the relationship between increased thermal history and phase transformation is still scant in most studies. Hence, a multi-scale FE model is required for HSM to assess how stress-strain and thermal fields affect phase changes within the material. Consequently, limited research has focused on establishing an FE model for the milling process, particularly one that encompasses phase transitions for both phases.

Hence, the current research objective is to investigate the phase transformation in two different stages during the HSM of Ti–6Al–4V. In the first stage (i.e., rapid heating), Avrami and Clapeyron-Clapeyron (C–C) type equations were implemented to predict α-to β-phase conversion by considering the stress-strain and temperature effects. While in stage two (i.e., rapid cooling), an empirical equation was implemented for the prediction of decomposed β-phase to α'-phase. The structured phase transitions model was implemented into the user-define VUSDFLD subroutine, employing a simplified FE model.

Finally, experiments were conducted on the HSM to validate and correlate the established thermo-metallo-mechanical model.

2. Phase transformation kinetics

Since the temperature history, higher stresses and cooling rates induced by HSM have considerably influenced the phase transformation in Ti–6Al–4V. Therefore, to realize the effect of heating and rapid cooling process separately, two sub-models for HSM of Ti–6Al–4V were carried out in the current investigation. Generally, temperature and increased stress are considered the fundamental aspects assisting the phase transformation of Ti–6Al–4V during the heating stage [17]. In contrast, abrupt temperature change rates are the main factor preceding phase conversion in rapid cooling [18]. Detailed implementation of these two processes (i.e., rapid heating and cooling) are described below.

2.1. Rapid heating process

Generally, as the temperature ascends to the initial point of the transition temperature, the α-phase undergoes a gradual conversion to the β-phase until it reaches 100% at the transus temperature, which is approximately 982.5 °C. Moreover, in Ti–6Al–4V, conversion from α-to β-phase requires the inauguration of β-phase from α-matrix and growth of β-phase through diffusion. Hence, to describe the β-phase volume fraction and the machining-induced cutting temperature, the Avrami model was implemented [19], which is expressed by Eq. (1).

$$V_\beta = 1 - \exp\left[A.\left(\frac{T - T_i}{T_c - T_i}\right)^D\right] \tag{1}$$

Where T, T_i, and T_c are the current deformation temperature, starting temperature for β-Ti transformation, and the complete phase transition temperature, respectively. Ti–6Al–4V starting and complete phase transition temperatures were set at 600 °C and 982.5 °C, respectively. Similarly, the terms A and D in Eq. (1) are the material constants that were set at −1.86 and 4.35, respectively [11,20].

Besides thermal history, the material phase transformation is also associated with the mechanical loads, which can categorically influence the formation of β-phase. Since the β-phase development within the α-matrix is a non-diffusion transformation process similar to martensite phase transformation [21]. Therefore, owing to linked proceedings of thermo-mechanical loads on Ti–6Al–4V during HSM, the transition of α-to β-phase is regarded as a martensite phase transformation. The quantitative relation between critical temperature and the critical stress as an external mechanical load of the initial phase transformation is expressed by employing the Clausius-Clapeyron type equation [22], as described in Eq. (2).

$$\frac{d\sigma}{dT_i} = -\frac{\rho \Delta H_{tr}}{T_0 \varepsilon_t} \tag{2}$$

in Eq. (2), ρ represents the mass density, ΔH_{tr} is the latent heat of transformation from α-Ti to β-Ti (taken as 4.18 kJ/mol) [23], T_0 is the equilibrium temperature, and ε_t is the transformation strain in the uniaxial stress direction.

2.2. Rapid cooling process

As the cutting tool advances into the workpiece material, the removed chips and machined surface go into the rapid cooling stage, and the volume of β-phase decomposition could result in a martensite with a microstructure of α' (with hexagonal structure) or α" (with orthorhombic structure) depending on the cooling rates. If the cooling rate is greater than or equal to 410 °C s^{-1} and the temperature (T) is less than martensitic transformation temperature (T_{MS}), the α' with martensite
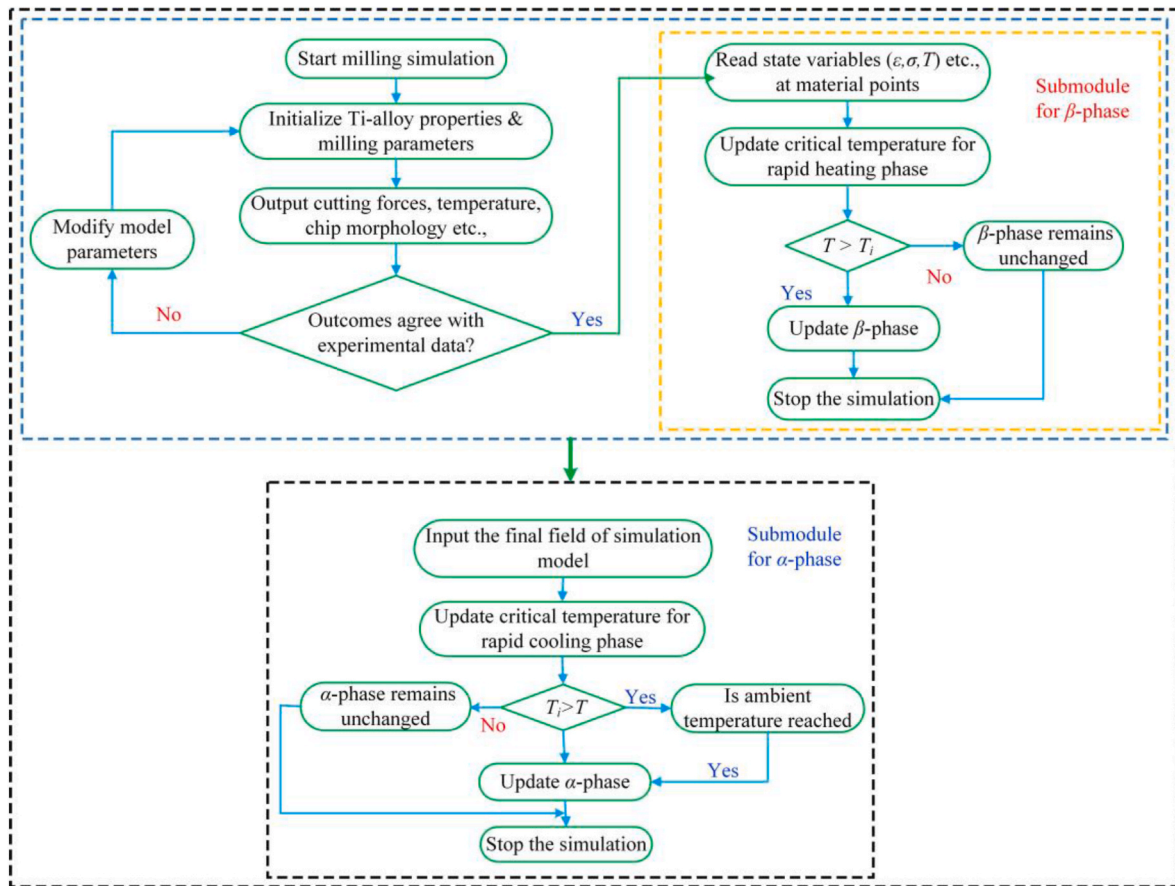
Fig. 1. Flowchart for predicting the phase transition during rapid heating and cooling process.

microstructure will form. In the current simulation, the critical cooling rate was set equal to 410 °C s^{-1}, notably slower than the cooling rates during the HSM (10^5 °C s^{-1}). Hence, it is assumed that α' will form. As a result, as described in Eq. (3), an empirical formula was adopted to estimate the volume fraction of α'-phase with an orthorhombic structure [14,24].

$$V_{\alpha'} = (V_\beta).(1 - \exp(1 - X(T_{MS} - T)))$$ (3)

Where V_β and T_{MS} demonstrate the amount of β-phase available for martensitic transformation following the heating process and the martensitic transformation temperature, respectively. X is the material constant, demonstrating the martensitic transition rate. The researchers have proven that approximately 10% of the β-phase remained unchanged, irrespective of the cooling rate, once the β-phase had undergone cooling to ambient temperature [25,26]. As a result, the value of X is set to 0.005.

2.3. Implementation of phase transformation models

The user-defined subroutine VUSDFLD was utilized to integrate rapid heating and cooling stages transition models into the simplified milling model. Fig. 1 illustrates a flow chart showcasing the sequential stages of submodules within the computational system.

The phase transitions simulation was achieved by utilizing two user subroutines. The temperature stress-strain field distributions for Ti–6Al–4V were retrieved from a validated simulated model during the rapid heating process. Subsequently, the volume fraction of β-phase was determined utilizing equations (1) and (2), respectively. Finally, the concluding field states from the heating stage were introduced to the cooling process model, and the volume percentage of α'-phase was

Table 1
JC material constitutive model and failure parameters for Ti–6Al–4V [28].

A(MPa)	B(MPa)	n	m	C	T_{room} (°C)	T_{melt} (°C)
860	683	0.47	1	0.035	20	1605
d_1	d_2	d_3	d_4	d_5		
−0.09	0.25	−0.5	0.014	3.87		

determined using equation (3).

3. FE model descritpion

3.1. Material constitutive model for Ti–6Al–4V

In this study, the Johnson-Cook (JC) constitutive material model (Eq. (4)) was employed to simulate the plastic behavior of Ti–6Al–4V. This model states the equivalent flow stress (σ) as a function of plastic strain (ε), strain rate ($\dot{\varepsilon}$), reference strain rate ($\dot{\varepsilon}_0$), and temperature (T) [27]. Similarly, a J-C fracture model was utilized for the chip formation process, as described in Eq. (5).

$$\sigma = (A + B\varepsilon^n)\left[1 + C \ln \frac{\dot{\varepsilon}}{\dot{\varepsilon}_0}\right]\left[1 - \left(\frac{T - T_{room}}{T_{melt} - T_{room}}\right)^m\right]$$ (4)

$$\overline{\varepsilon}_f^{pl} = [d_1 + d_2 \exp(-d_3)\eta]\left[1 + d_4 \ln\left(\frac{\dot{\varepsilon}^{pl}}{\dot{\varepsilon}_0}\right)\right]\left(1 - d_5\widehat{\theta}\right)$$ (5)

In Eq. (4), the terms *A, B, C, n,* and *m* are the initial yield strength, hardening modulus, strain rate sensitivity, strain rate hardening exponent, and thermal softening coefficient, respectively. While in Eq. (5), the terms d_1-d_5 are the failure factors, η represents the deviatoric stress
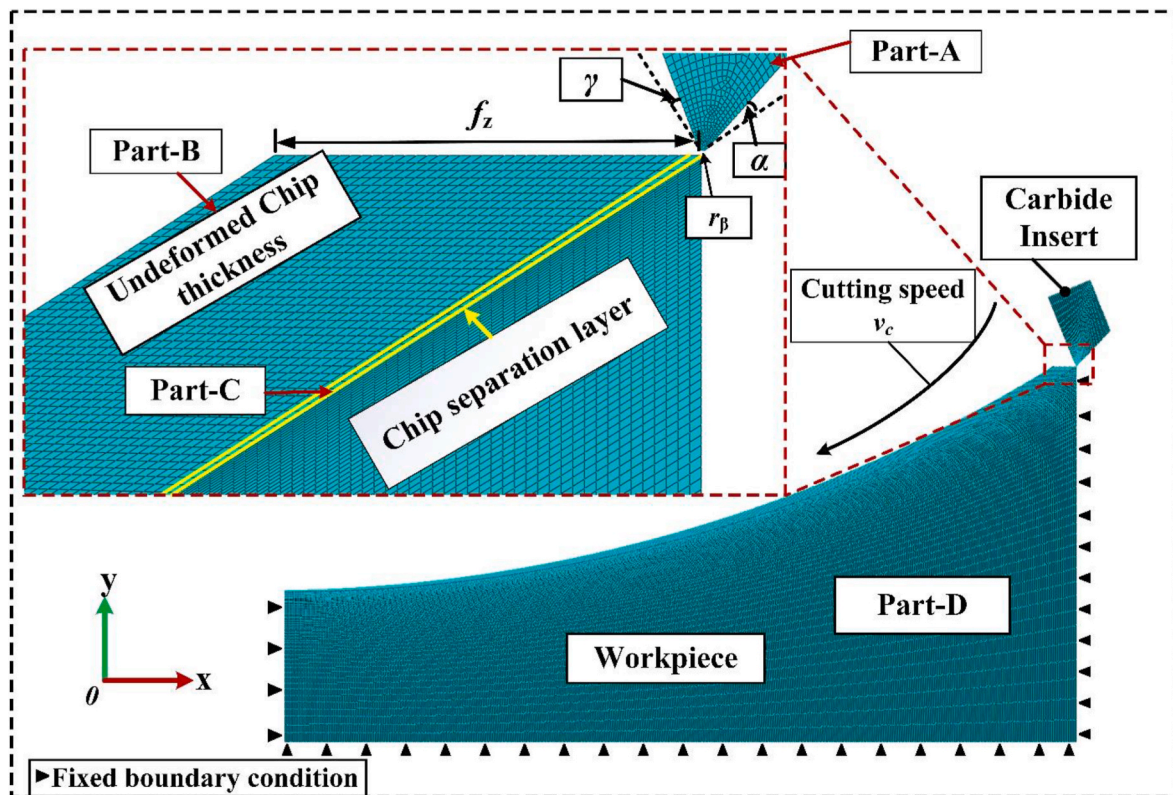
Fig. 2. Simplified FE model for HSM of Ti–6Al–4V.

ratio and $\widehat{\theta}$ is a dimensionless thermal partition. Table 1 displays the values attributed to the J-C constitutive model along with the consequent failure parameters pertinent to the Ti–6Al–4V material.

3.2. Initial boundaries conditions and meshing

A precise FE model is crucial for accurately capturing and comprehending the phase changes in Ti–6Al–4V. Fig. 2 depicts a developed milling model that has been verified in the author prior research [28]. As indicated, the workpiece was constrained from three sides, and the physical parameters and geometry of the cutting tool remained identical to those utilized in the machining tests. The workpiece and cutting insert were meshed by assigning element type CPE4RT, which combines plain stain quadrilateral with temperature-displacement coupling. The initial

temperature for the workpiece and cutting insert was equivalent to 20 °C, and the inelastic heat fraction was set as 0.9 to describe the heat flux flows into the chip.

Since the HSM involves complex physical phenomena, including material deformation, chip formation, and heat generation. Therefore, an accurate contact model is required to represent the interaction between the workpiece and the cutting tool. A Zorev model was incorporated in the current simulation to illustrate the sliding and sticking behavior between the chip-tool interface [29].

$$\tau_f = \begin{cases} \mu\sigma, \mu\sigma \leq \tau_{crit} \text{ (sliding zone)} \\ \tau_{crit}, \mu\sigma \geq \tau_{crit} \text{ (sticking zone)} \end{cases} \tag{6}$$

Where τ_f, τ_{crit}, μ, and σ are the frictional shearing stress, critical shear stress, friction coefficient, and normal stress, respectively. In the current
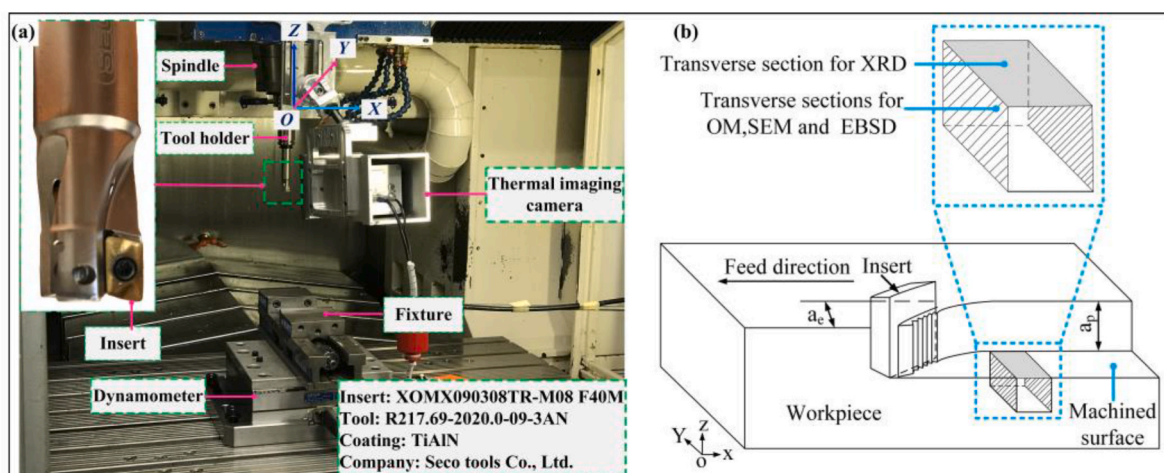

Fig. 3. Experimental setup for HSM: (a) machining setup, (b) metallographic test areas.
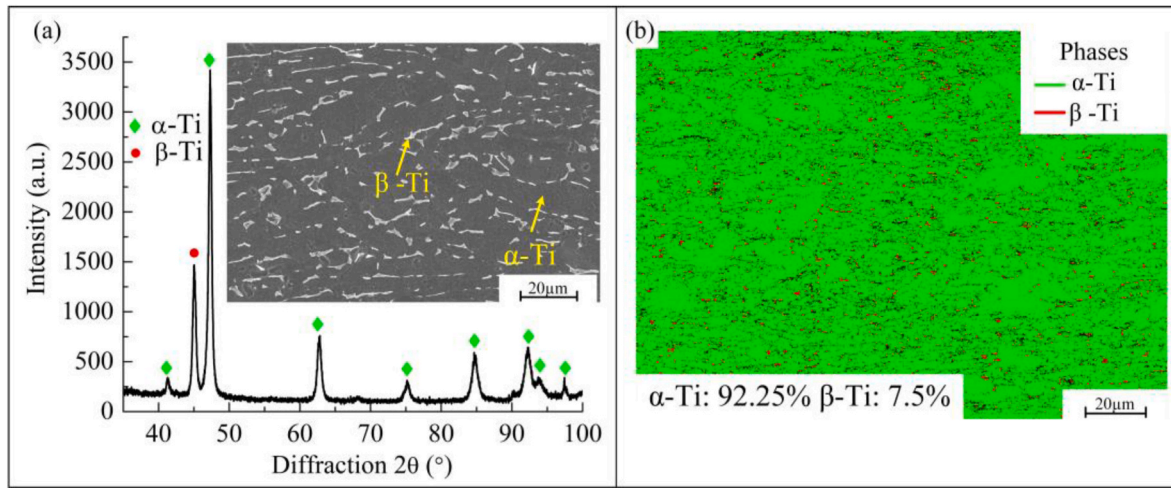
Fig. 4. Initial microstructural and phase composition of the base material.

Table 2
Detailed experimental setup for HSM of Ti–6Al–4V.

Exp nos.	Cutting speed v_c(m/min)	Radial depth of cut a_e(mm)	Axial depth of cut a_p(mm)	Feed per tooth f_z (mm/z)
1#	150	1.6	1.4	0.20
2#	250	1.6	1.4	0.20
3#	350	1.6	1.4	0.20
4#	150	1.6	1.4	0.15
5#	150	1.6	1.4	0.20
6#	150	1.6	1.4	0.25

research, the coefficient of friction was set at 0.24, according to the author's previous research [28].

4. Experimental work

Ti–6Al–4V with chemical composition of 6.11–6.14 wt% Al, 3.89–4.01 wt% V, 1.4–2.6 wt% Sn, 0.31–1.1 wt% Fe, 0.34–90 wt% Cu was employed as a material test for the HSM. Tests were carried out in a dry environment on a 3-axis vertical machining center (Huron K2X10).

A Kistler piezoelectric dynamometer (type 9255B) and thermal imaging camera were employed to record the cutting forces and temperature. As depicted in Fig. 3(a)–A PVD-coated carbide insert, held tightly with a milling cutter, was used during machining tests. To mitigate the impact of tool wear on surface integrity, a new milling insert was utilized for every experiment.

Upon completion of the milling experiments, samples measuring 7 mm^3 in dimensions were extracted from the machined surface for subsequent metallographic observation, as delineated in Fig. 3(b). Finally, a combination of advanced characterization instruments such as optical microscopy (OM), Electron Backscattered Diffraction (EBSD), scanning electron microscopy (SEM), and X-ray diffraction analysis (XRD) were utilized for comprehensive analysis and observation. These were used to assess the geometrical and microstructural state of the machined surface and removed chips.

4.1. Base material microstructural and phase compositions

Fig. 4 depicts the microstructures and phase composition of as-received Ti6Al4V. This alloy was received in the form of plates which were obtained by cold rolling.
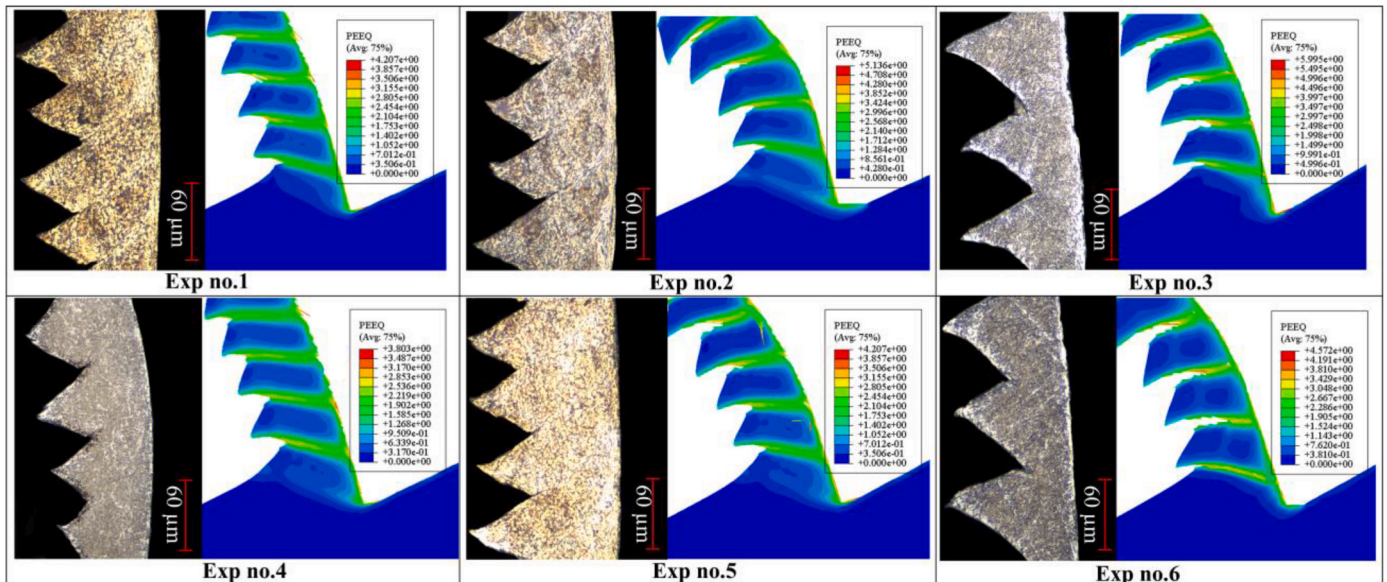

Fig. 5. Chip morphology comparison between experiment and simulation.

Table 3
Detailed comparative results of chip geometrical characteristics.

Exp nos.	Value	Chip Morphology (μm)		
		Average Peak	Average Valley	Average Spacing
1#	Simulated	76.86	54.63	62.13
	Experimental	80.56	59.23	56.47
	Relative error (%)	6.03	8.42	9.11
2#	Simulated	82.53	46.36	60.91
	Experimental	88.23	51.67	57.77
	Relative error (%)	6.90	11.45	5.15
3#	Simulated	82.23	42.36	65.26
	Experimental	87.74	37.36	73.39
	Relative error (%)	6.7	11.80	12.46
4#	Simulated	73.36	56.30	45.23
	Experimental	77.16	52.26	49.39
	Relative error (%)	5.42	7.17	9.19
5#	Simulated	76.86	54.63	62.13
	Experimental	80.56	59.23	56.47
	Relative error (%)	6.03	8.42	9.11
6#	Simulated	85.53	40.36	68.82
	Experimental	79.23	45.23	74.56
	Relative error (%)	7.36	12.06	8.34

Footnote: % relative error = | (simulated value – experimental value)/simulated value |

XRD and EBSD analysis indicated that the base material mainly comprised 92.25% α-Ti and 7.5% β-Ti. The α-phase has a hexagonal-close-packed (HCP) crystal structure, while the crystal structure of the β-phase is a body-centered cubic (BCC).

4.2. FE model validation

To validate the accuracy of an established model, six experimental trials were selected (given in Table 2). First, the developed model was verified regarding chip geometrical characteristics(i.e., peak, valley, and spacing). As shown in Fig. 5, a serrated chip was consistently observed for all the experimental trials, and the simulated chip morphology was adequately coherent with the experimental findings.

For a detailed elucidation of chip morphology, the geometrical features of serrated chips were determined and analyzed, and the obtained results are documented in Table 3. As listed, the average relative error of the three features (i.e., peak, valley, and spacing) obtained through

simulation and experiment is less than 13 %, which proves the reliability and precision of the established FE model.

Similarly, to further verify the developed model, the simulated and experimental cutting forces values were compared in Fig. 6. As presented in Fig. 6(a) and (b), the experimental cutting forces in X and Y direction for Exp nos. 1, 2, and 4 are slightly higher than the simulated ones. In contrast, for Exp nos. 3, 5, and 6, the simulated cutting forces dominated the experimental ones in the X-direction, while opposite trends were absorbed for cutting forces in the Y-direction.

Furthermore, it was also observed that experimental cutting forces in the X-direction first increased with cutting speed (i.e., Exp nos. 1 and 2) and feed rates (i.e., Exp nos. 4 and 5) and then declined with further increase in cutting speed (Exp no.3) and feed rate (Exp no.6). The percentage relative to cutting forces in both directions was less than 14.2%. These analyses indicated that the developed FE model of Ti–6Al–4V is accurate and reliable. Therefore, it can simulate phase transformation under a coupled thermo-metallo-mechanical effect.

5. Results and discussion

5.1. Analysis of phase transformation during rapid heating

The simulated outcomes for equivalent plastic strain, von Mises stress, temperature, and β-phase volume fraction for three experimental trials are demonstrated in Fig. 7. As indicated in Fig. 7(a–c), the predicted maximum equivalent plastic strain were about 4.2, 5.15, and 5.99 for Exp nos. 1,2, and 3, respectively. On the one hand, the plastic strain was relatively higher in the primary and secondary deformation zones and at the tool-workpiece interface. On the other hand, the plastic strain at the milled surface is significantly lower compared to that observed at the shear plane and chip back surface. The higher plastic strain is mainly contributed by severe plastic deformation [30]. Fig. 7(d–f) shows that the highest stress values were concentrated within the primary shear zone, reaching approximately 1941 MPa, 2219 MPa, and 2372 MPa for Exp nos. 1, 2, and 3, respectively. Furthermore, it can also be observed from the silhouette that the maximum stress values on the machined surface were limited to 500 MPa for all the experiments. Meanwhile, in machined subsurface zones, the stress values lie in the range of 970 MPa to around about 1780 MPa for all the experiments.

Similarly, higher temperatures are another prerequisite for assisting the phase transitions. The simulation outcomes of temperature fields during the HSM of Ti–6Al–4V have been indicated in Fig. 7(g–i). As shown, when the tool crosses the shear plane of the material, the temperature significantly rises from room temperature. The extreme heat generation can be primarily attributed to severe shear plastic deformation, leading to higher temperatures in the cutting deformation zones
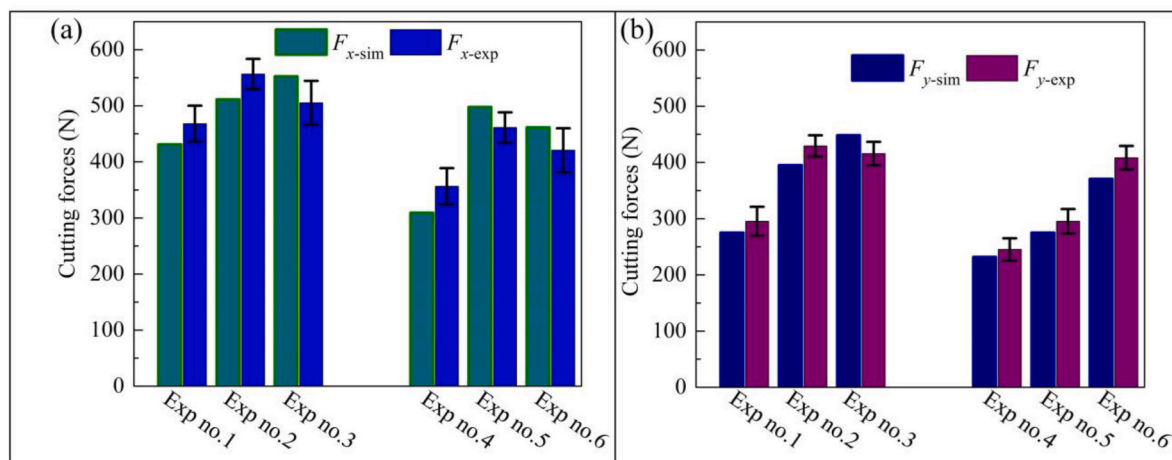

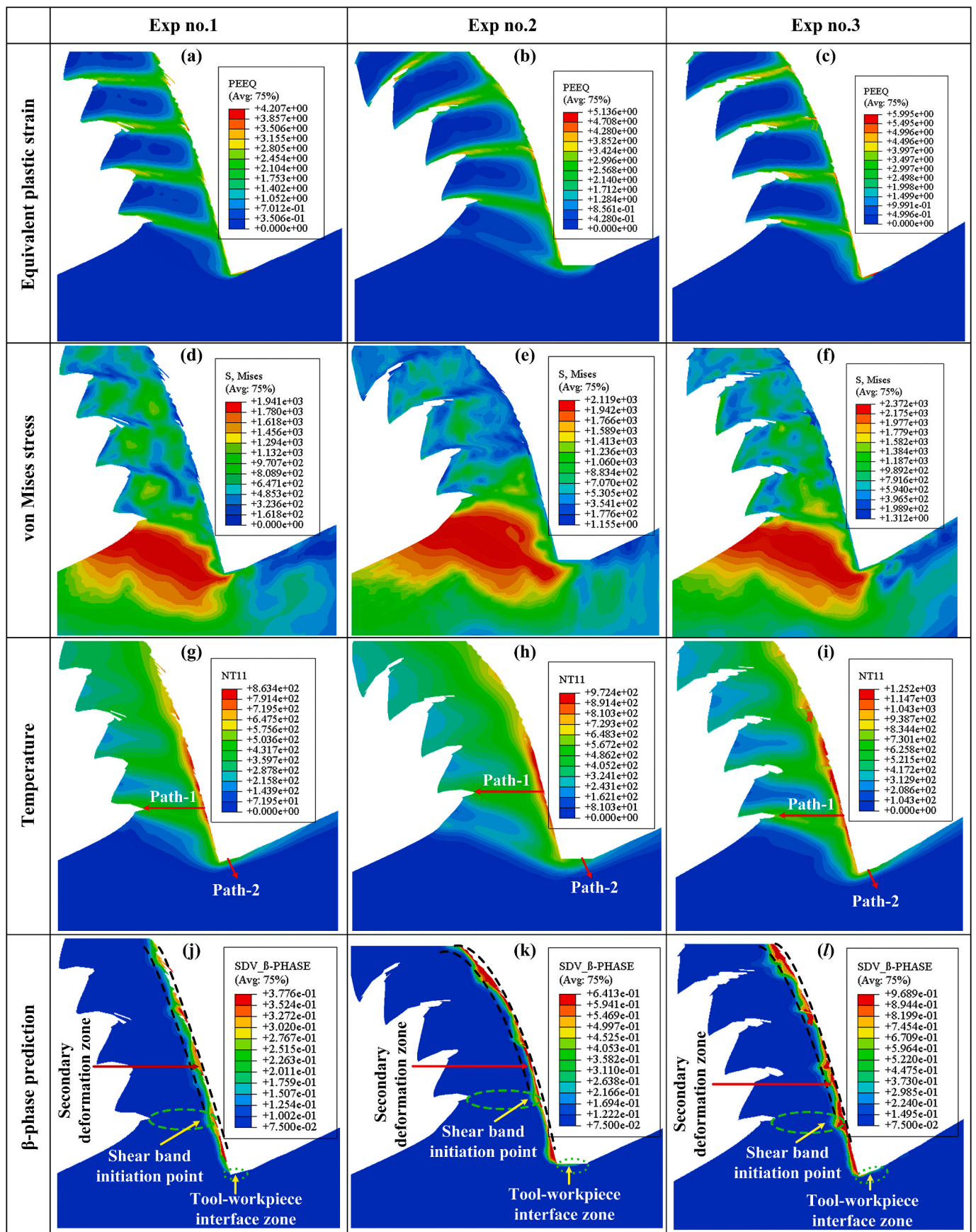**Fig. 6.** Experimental and simulated cutting forces comparison.

Fig. 7. Prediction of plastic stain, von Mises stress, temperature, and β-phase field for Exp no. 1,2 and 3.
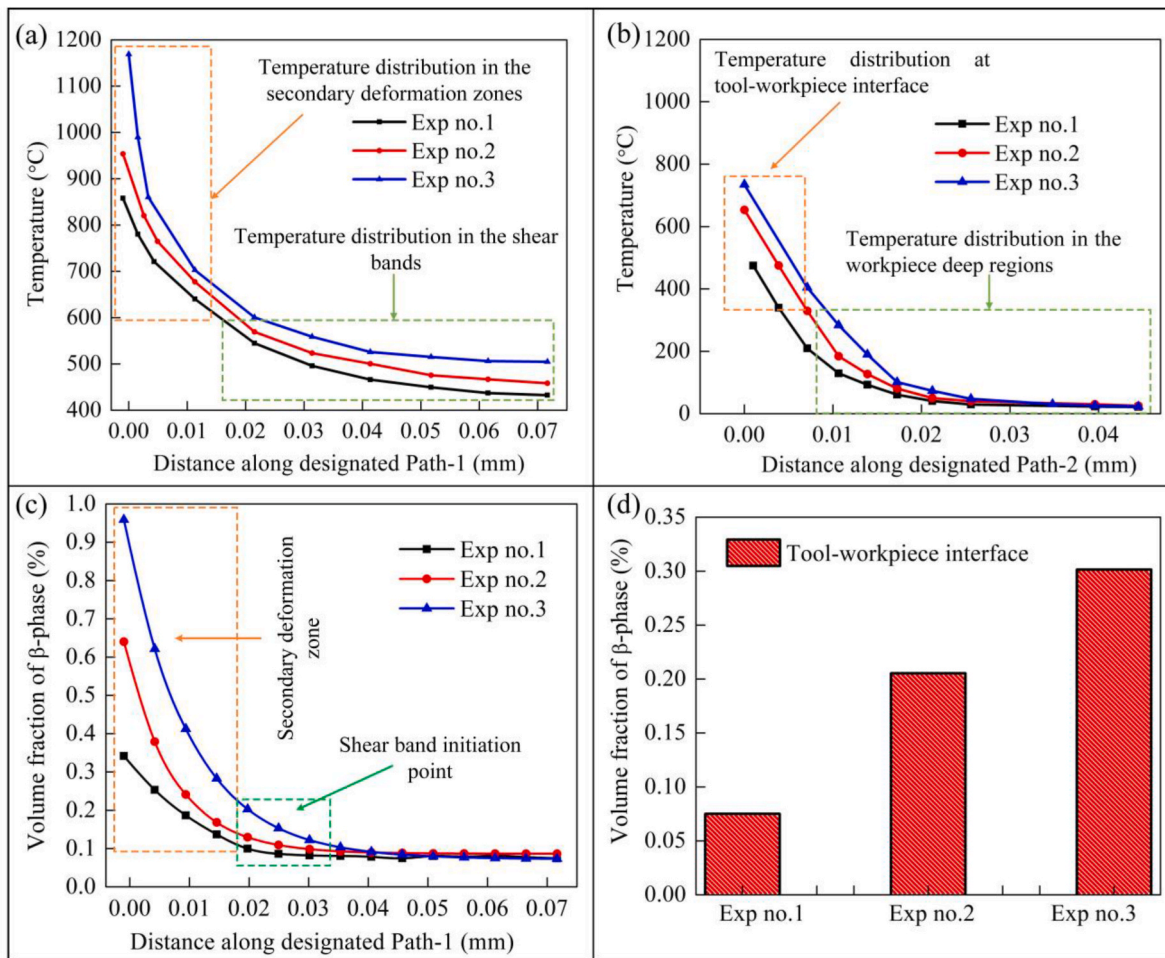
Fig. 8. Temperature and corresponding β-phase for Exp nos. 1,2 and 3: (a–b) temperature variation along path-1 and path-2, and (c–d) volume fraction of β-phase along path-1 and path-2.

[31].

For a detailed understanding of temperature distribution within the cutting deformation zones, two paths (i.e., Path-1 and Path-2) were generated within the shear band and at the tool-workpiece interface, as shown in Fig. (g–i), and the obtained results were plotted in Fig. 8(a and b). As displayed in Fig. 8(a), the maximum temperature was allocated in the secondary deformation zones (i.e., chip back surface). It can be seen that temperature dramatically enhances from ambient temperature to 863.4 °C (Exp no.1), 972.4 °C (Exp no.2), and 1252 °C (Exp no.3), respectively, and decreases cyclically within the shear band. Similarly, as indicated in Fig. 8(b), the maximum temperature at the tool-workpiece interface was about 474.7 °C (Exp no.1), 653.5 °C(Exp no.2), and 734.7 °C, respectively.

The predicted phase transformation (i.e., from α-to β-phase) has been indicated in Fig. 7(j-l). Notably, the primary volume percent of β-phase was adjusted, equivalent to 7.5%. According to the results shown in Fig. 7(j–l), a shallow layer in the chip back surface has undergone a phase transformation (i.e., α-to β-phase). As mentioned earlier, thermal history has a predominant role in phase transformation. Therefore, as seen in Fig. 8(c), when the temperature in the chip back surface was about 863.4 °C (for Exp no.1), the volume percentage of β-phase was increased from 7.5 % to about 33.5 %. In comparison, when the temperature reached 972.4 °C, the β-phase volume fraction was enhanced to 63.56 % (Exp no.2). Similarly, with further increase in cutting speed (i. e., 350 m/min (Exp no.3)), the temperature in chip back surface rises to 1252 °C and almost all of the α-phase has been transformed into β-phase (Fig. 8(c)). Similarly, as indicated in Fig. 8(d), when the peak

temperature at the tool-workpiece interface was about 471.72 °C, no changes in β-phase were detected for Exp no.1, while for Exp nos. 2 and 3, when the peak temperature at the tool-workpiece interface reaches 653.58 °C, and 754.65 °C, the volume fraction of β-phase was increased to 20.53 % and 30.14 %, respectively.

Three additional tests (i.e., Exp no. 4,5 and 6) were conducted to further understand the consequence of feed rates on phase transition, and the obtained results were plotted in Fig. 9. It can be seen that the feed rates also affect the plastic strain, von Mises stress, temperature, and volume fraction of β-phase. As depicted in Fig. 9(a–c), when the feed rates were enhanced from 0.15 (Exp no.4) to 0.25 (Exp no.6), the plastic strain was increased from 3.80 to 4.57, and the von Mises stress was augmented from 1825 MPa to 2042 MPa (Fig. 9(d–f)), respectively. Fig. 9(g–i) indicates that the feed rates also influence the temperature. Again, the highest temperature was observed in the secondary deformation zones for all the experiments. As revealed in Fig. 10(a and b), the peak temperature at the chip's back surface (i.e., along Path-1) was about 789.53 °C, 858.05 °C, and 953.75 °C for Exp nos. 1,2 and 3, respectively. In contrast, the tool-workpiece interface temperature (along Path-2) was about 414.72 °C, 474.72 °C, and 659.65 °C, respectively.

The distribution of β-phase against various feed rates has been demonstrated in Fig. 9(j–l). On the one hand, when the temperature increased to 789.53 °C (Exp no.4), the β-phase volume fraction increased to 22.41%. Similarly, when the temperature surges to 858.05 °C (Exp no. 5) and 953.75 °C (Exp no.6), the volume percentage of β-phase proceeded to 33.5 % and 67.84 %, respectively, as shown in
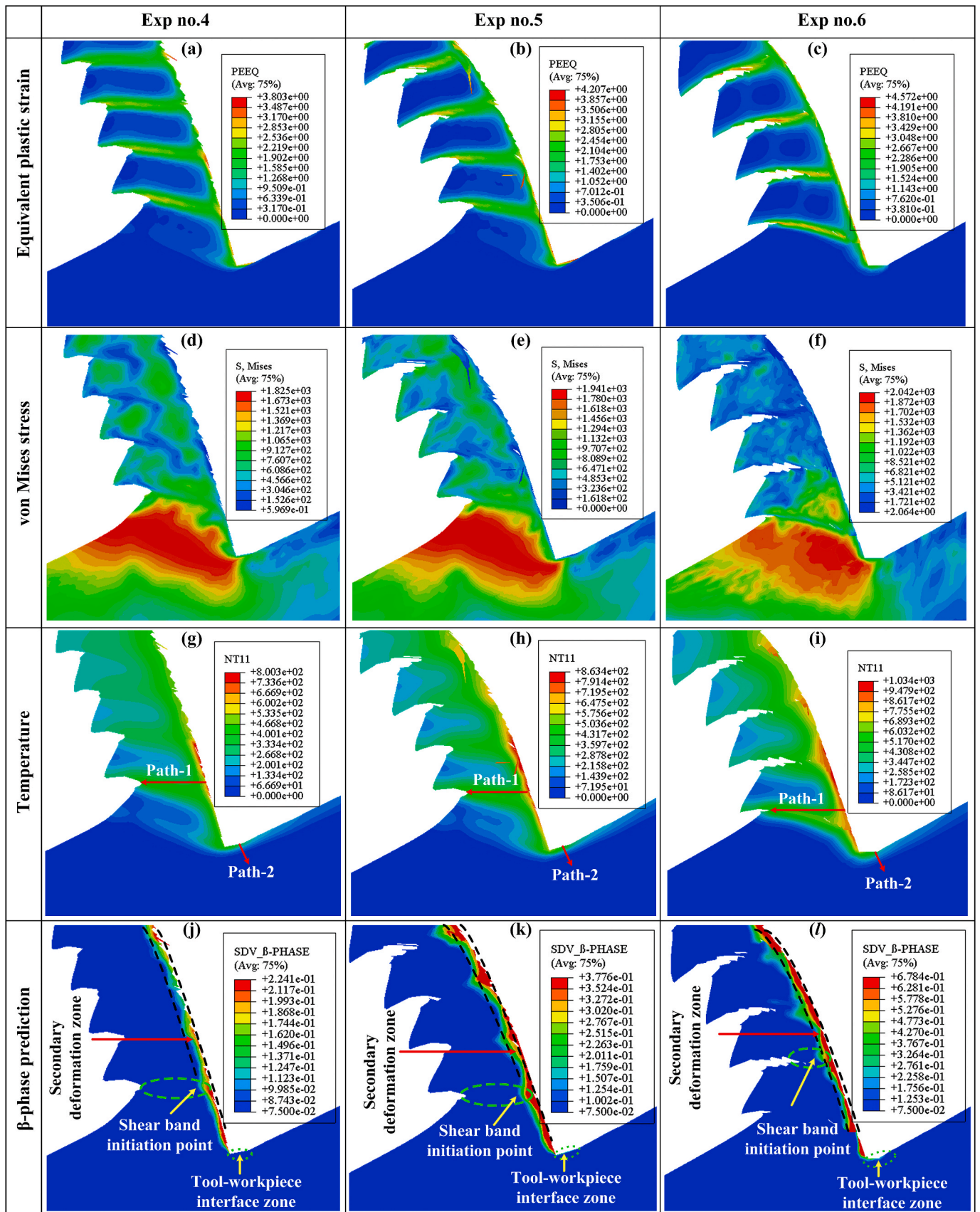
Fig. 9. Prediction of plastic stain, von Mises stress, temperature, and β-phase field for Exp no. 4,5 and 6.
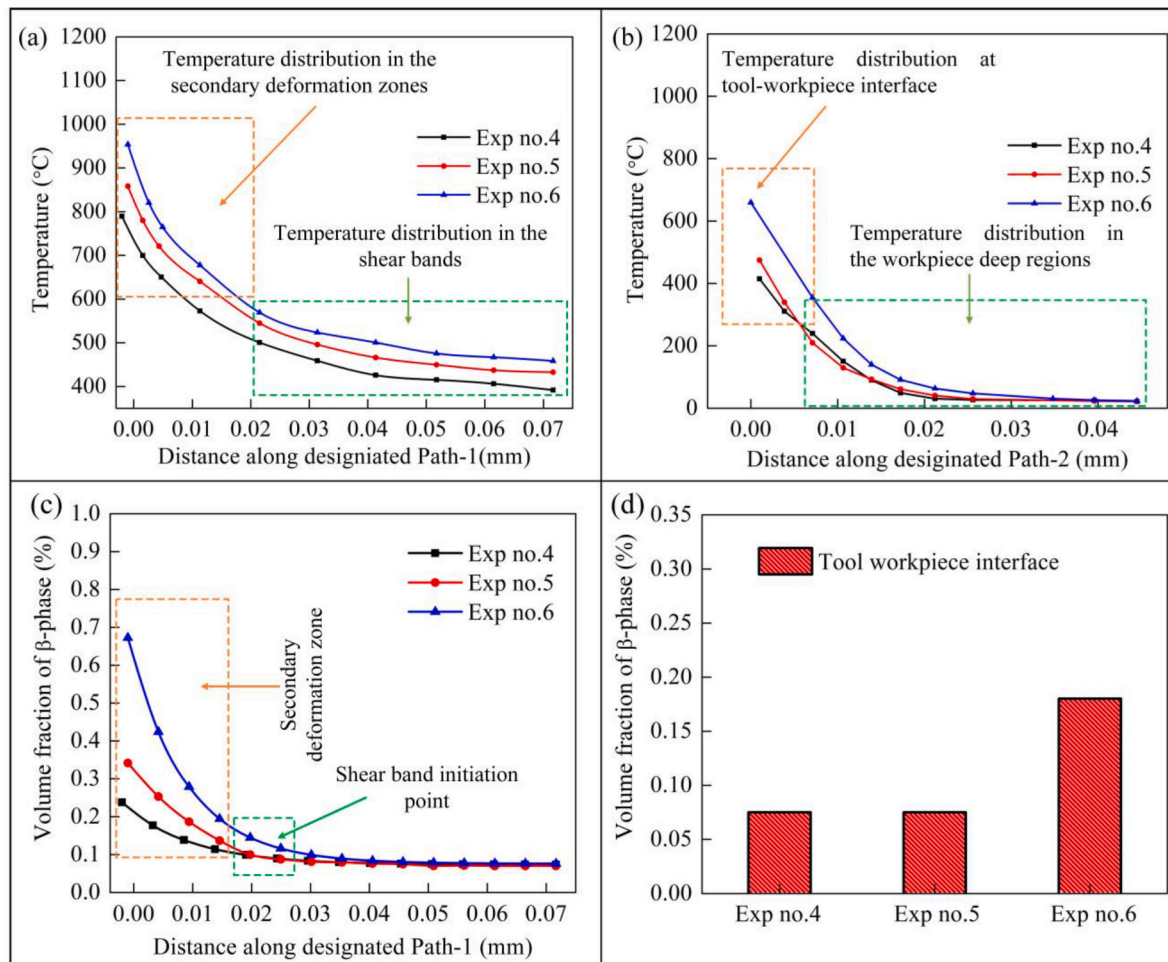
Fig. 10. Temperature and corresponding *β*-phase for Exp nos. 4,5 and 6: (a–b) temperature variation along path-1 and path-2, and (c–d) volume fraction of *β*-phase along path-1 and path-2.
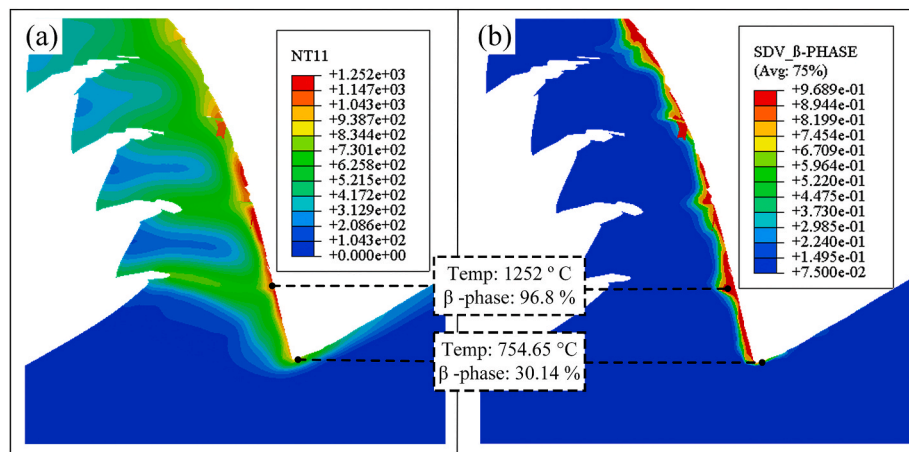

Fig. 11. Mapping relationship between *β*-phase field and temperature for the rapid heating stage.

Fig. 10(c). On the other hand, when the temperature at the tool-workpiece interface was about 414.72 °C (Exp no.4) and 474.72 °C (Exp no.5), respectively, no phase transformation occurred. However, when the temperature at the tool-workpiece interface increased to 659.65 °C for Exp no.6, the volume percentage of *β*-phase was increased to 17.5% (Fig. 10(d)).

As depicted in Fig. 11, a reasonably good correlation existed between

the simulated *β*-phase and the cutting temperature distribution. The distinct stress, strain, and cutting temperature distributions within the cutting deformation zones likely contributed to the inhomogeneous distribution of *β*-phase across different deformation zones due to their combined effects.

Moreover, no phase transformation was identified in the milled surface. This is because the machined surface is below the initial phase
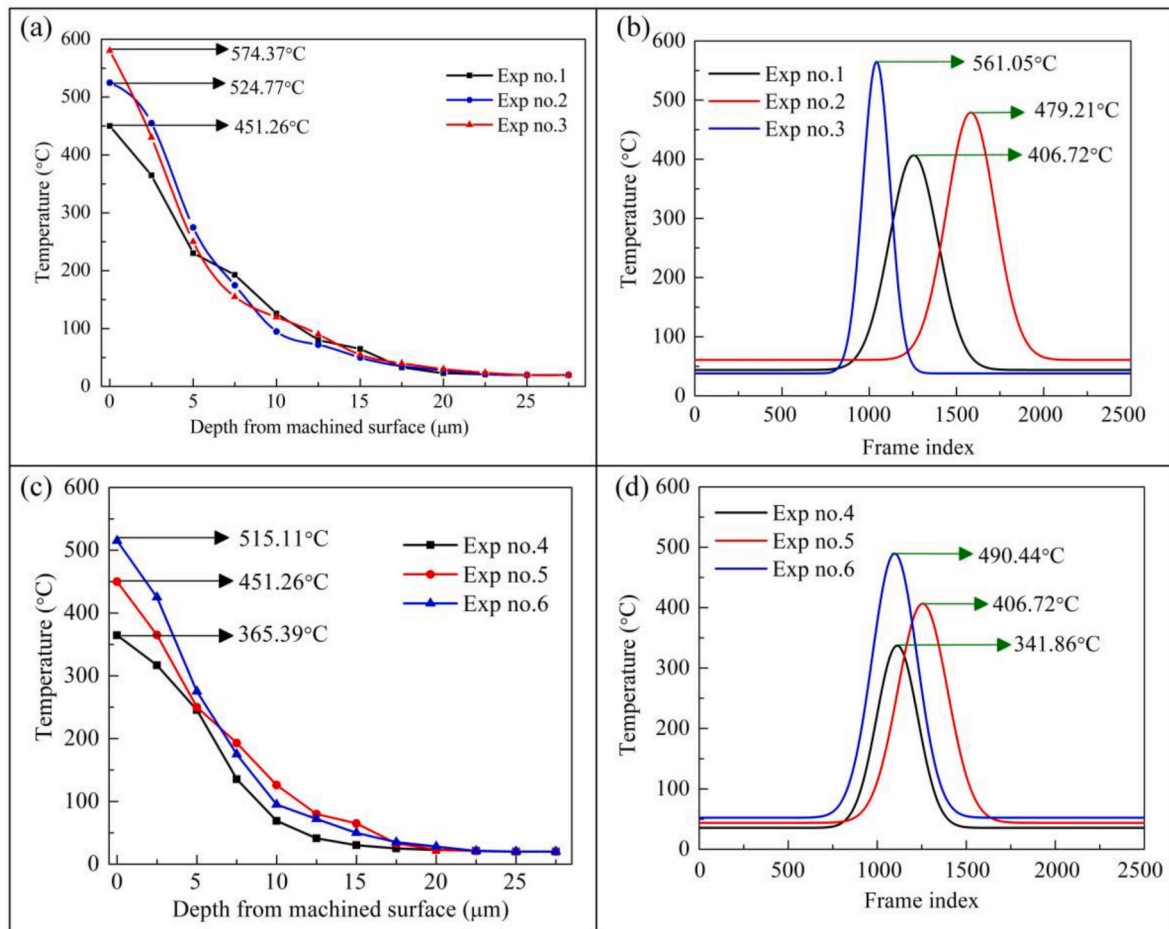
Fig. 12. Simulated and experimental machined surface temperature comparison.

transformation temperature. As depicted in Fig. 12 (a), the maximum machined surface simulation temperature for Exp no. 1,2 and 3 was 451.26 °C, 524.77 °C and 574.37 °C, respectively. In contrast, the temperature observed during the milling tests for these experiments was approximately 406.72 °C, 479.21 °C, and 561.05 °C, respectively. Similarly, the maximum simulated temperature of the machined surface for Exp nos. 4, 5, and 6 was 365.39 °C, 451.25 °C, 515.11 °C, while the maximum experimental machined surface temperature was 341.86 °C, 406.72 °C, and 490.44 °C, respectively.

As observed, the simulated machined surface temperature dominates the experimental ones for all the tests. Nevertheless, the machined surface temperature for both experimental and simulated temperatures is below the martensitic phase transformation temperature. Generally, the proportion of total heat transferred into a workpiece varied from 1% to 20%, which is significantly lower than the 74%–96% thermal energy ratios blown away by the chip [32]. In contrast to the chip, the stress and plastic strain distributions are relatively lower on the machined surface. Consequently, these combined conditions diminish the probability of the machined surface undergoing a phase transition.

5.2. Analysis of phase transformation during rapid cooling

Following the rapid heating stage, the volume percentage of α'-phases during the rapid cooling stage for various milling experiments has been conducted (Fig. 13). In the simulation results, the red regions represent the volume fraction of α-phase, while the blue areas indicate the volume fraction of α'-phases. Notably, all experiments consistently witnessed a substantial volume fraction of α'-phase in the chip's back surface. However, for Exp no.1, 4, and 5, no α'-phases were detected at

the tool-workpiece interface since, for these experiments, the β-phase did not change during the first stage. It can be seen that the α'-phase distributes homogeneously in the secondary deformation zones. For Exp no.1, the volume fraction of α'-phases was about 9.5% at the chip back surface region, while for Exp no.2 and 3, the volume fraction of α'-phases reduced to 8.76 and 7.81 %, respectively. Similarly, when the feed rate increased from 0.15 to 0.25 mm/tooth (i.e., Exp no.4 to Exp no.5), the percentage volume fraction of α'-phases was reduced from 9.69 to 8.35, respectively.

On the one hand, the increased heat generation due to higher cutting speeds (Exp nos. 1–3) can shorten the time available for phase transformation and significantly change the kinetics and completeness of martensitic transformation, specifically the volume fraction of α' phase. On the other hand, increased feed rates cause more frictional forces between the cutting tool and the workpiece, resulting in more heat energy, which surges the transformation process. However, the decreased period for phase transition may slow down the complete reconversion of the β-phase, resulting in a smaller volume percent of the α'-phases. Furthermore, higher feed rates originate sharp heat gradients within the material, altering diffusion rates and microstructural development, which affects martensitic grain nucleation and growth.

A mapping illustration in Fig. 14 showed a vital observation. As demonstrated, the regions where the β-phase encountered during the heating stage were reconverted back into α'-phases during the subsequent rapid cooling step. This finding emphasizes the dynamic character of the material's behavior during machining under various thermal conditions. The reversible transition from β-phase to α'-phases throughout the heating and cooling stages provides information on the material's sensitivity to thermal fluctuations, offering vibrant insights
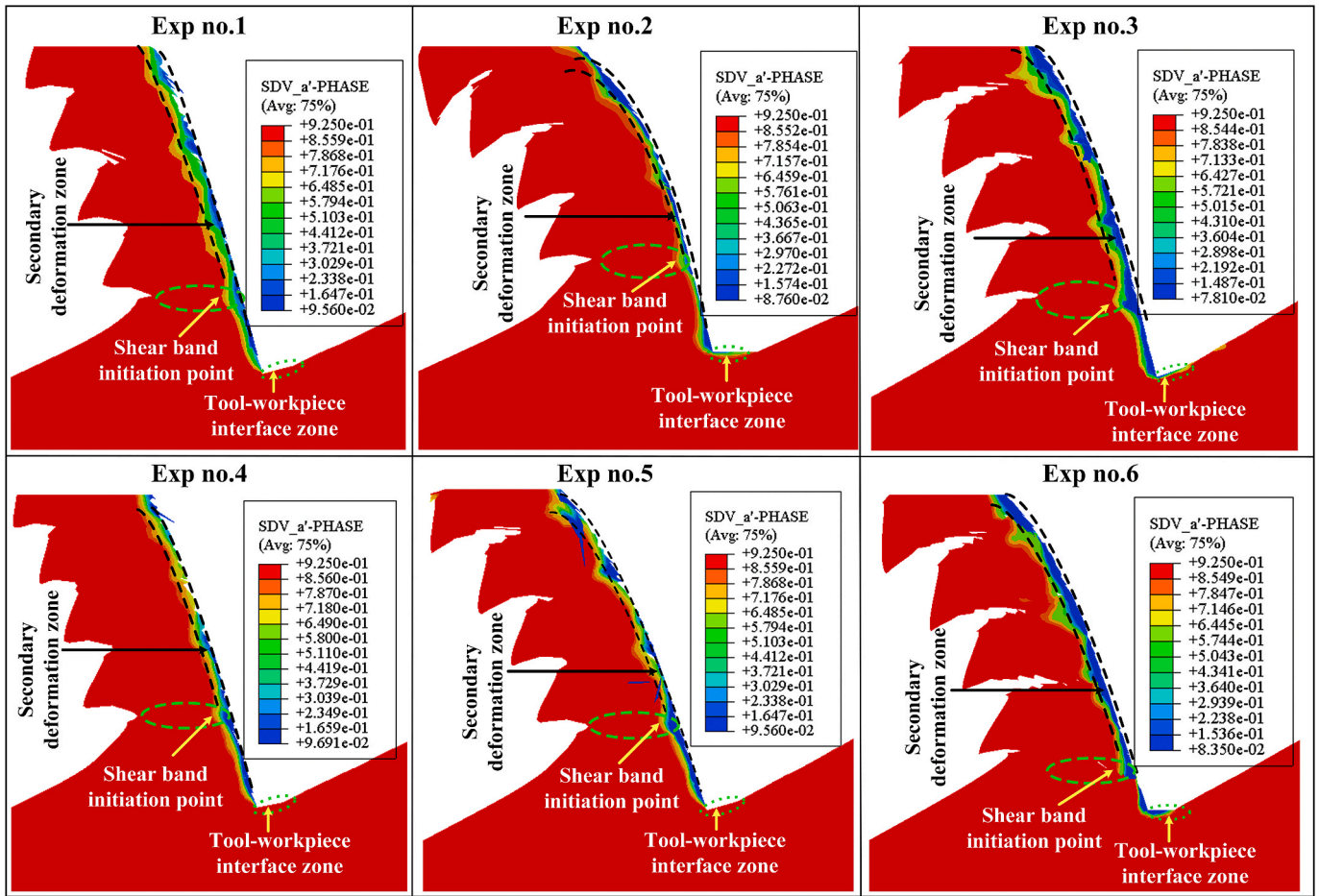
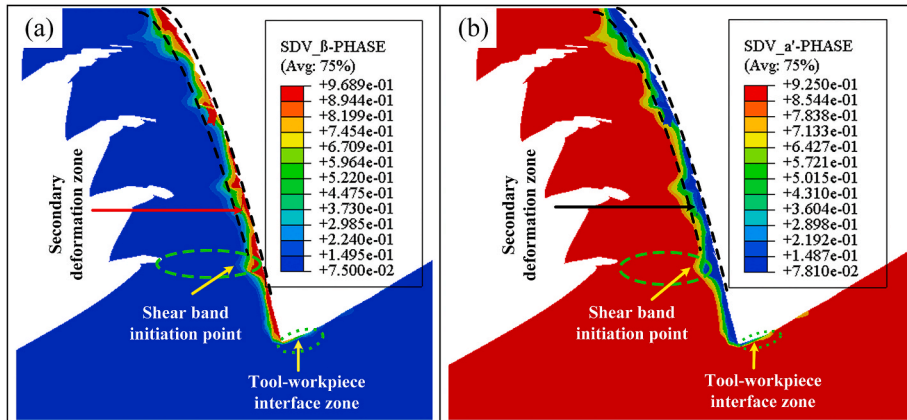Fig. 13. Evolution of α'-phases volume fraction during the rapid cooling process.

Fig. 14. Mapping correlations between β-phase and α'-phases for Exp no.3.

into the structural modifications of Ti–6Al–4V during the machining process.

5.3. Experimental validation of the developed model

Due to severe plastic deformation, Ti–6Al–4V experiences rapid heating in the cutting plane and subsequently undergoes quick cooling once the cutting insert advances into the workpiece. Consequently, the phase transformations occur in two stages within an extremely short period: first, the conversion from α-to β-phase during heating, followed

by the reverse transformation. Owing to the transient approach of high-speed milling, the β-phase within the cutting deformation zones is challenging to analyze directly during the actual machining experiments. Therefore, the simplified milling model was validated only during the rapid cooling stage in the current research by employing some advanced characterization techniques.

XRD analysis was conducted on the machined surface for all the selected experiments, and the results obtained were plotted in Fig. 15. Contrast to a base alloy, although the machined surface's phase compositions and relative peak intensities vary with changing milling input
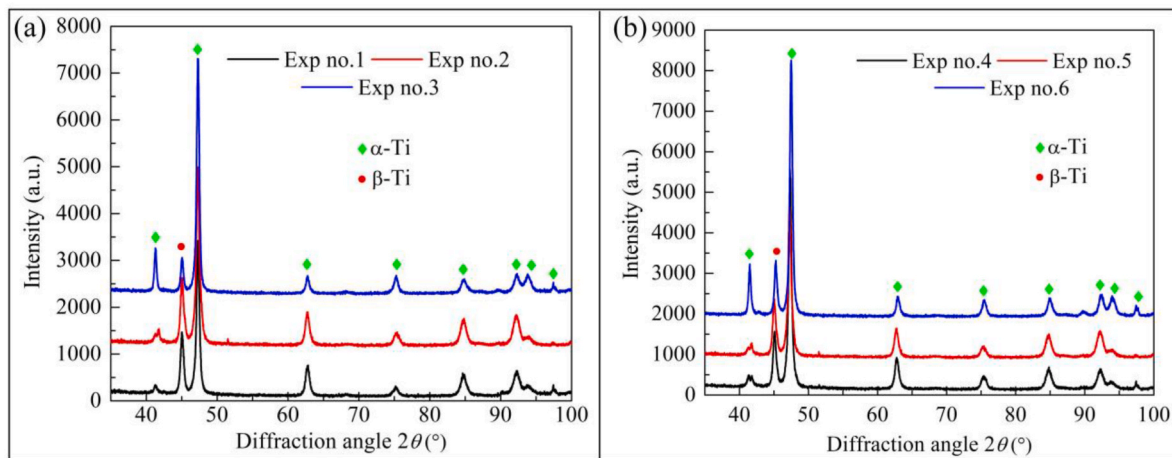
Fig. 15. XRD analysis of machined surfaces: (a) phase composition for Exp nos. 1, 2, and 3, (b) phase composition for Exp nos. 4, 5, and 6.
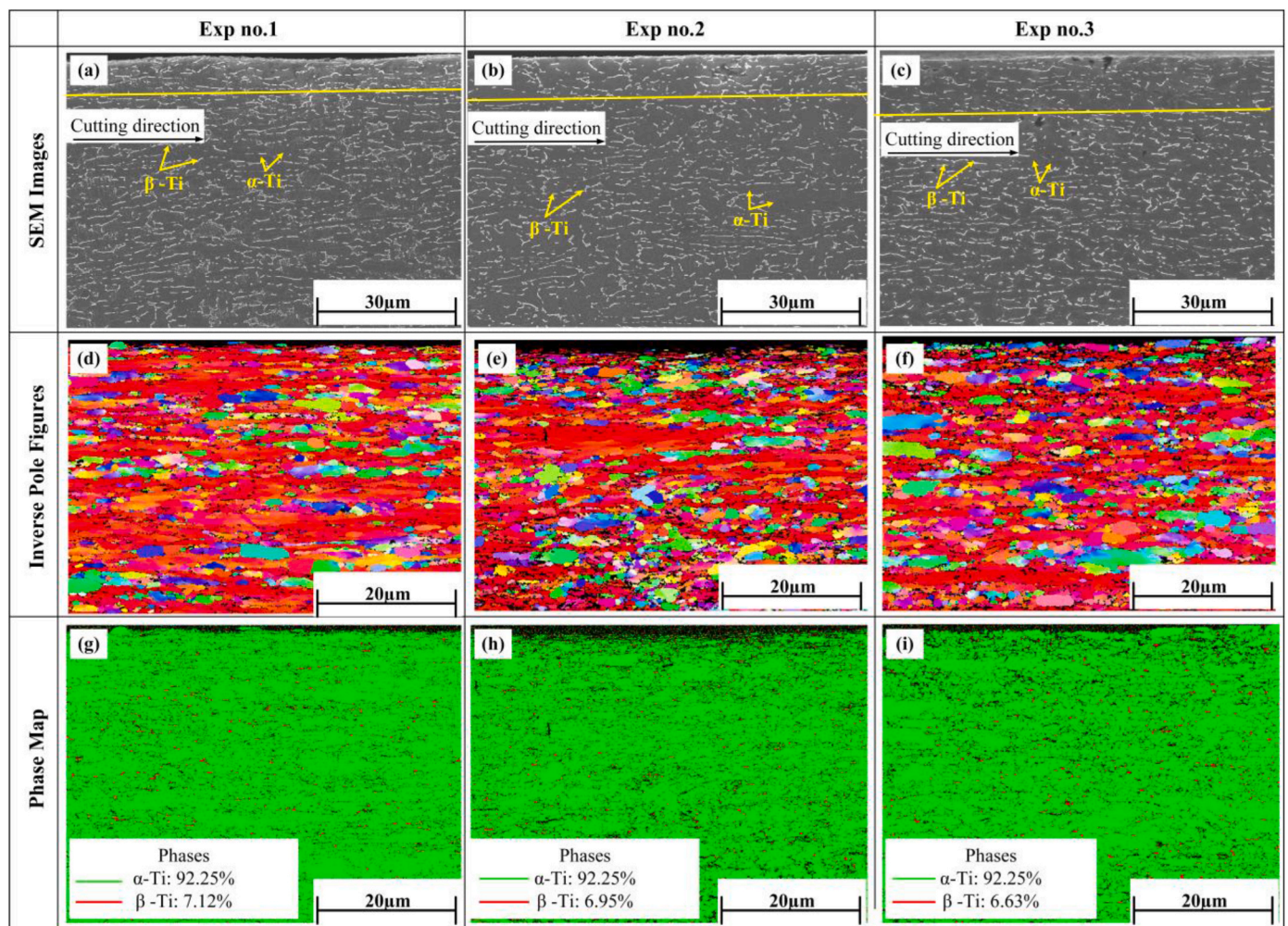

Fig. 16. SEM and EBSD results of machined surface layer: (a–c) SEM images, (d–f) Inverse pole figures for grain size evolution, and (g–i) phase map.

parameters; specifically, the peak intensities for the β-phase decreased, leading to a corresponding diminution in the volume fraction of β-phase. These peak intensities owing to the reduced crystalline size and perhaps nano-sized grains caused by the severe plastic deformation at the machined subsurface [33].

Furthermore, the material's grain size can affect the XRD peaks' full width at half maximum (FWHM) [34]. Smaller grain sizes generally result in broader diffraction peaks, while larger grain sizes produce sharper peaks. This is because smaller grains lead to a more pronounced distribution of diffraction angles due to crystallite orientation and size variations within the sample.

Nonetheless, the peak intensity positions remain consistent, which suggests that the machined surface has not significantly altered the crystallographic phases.
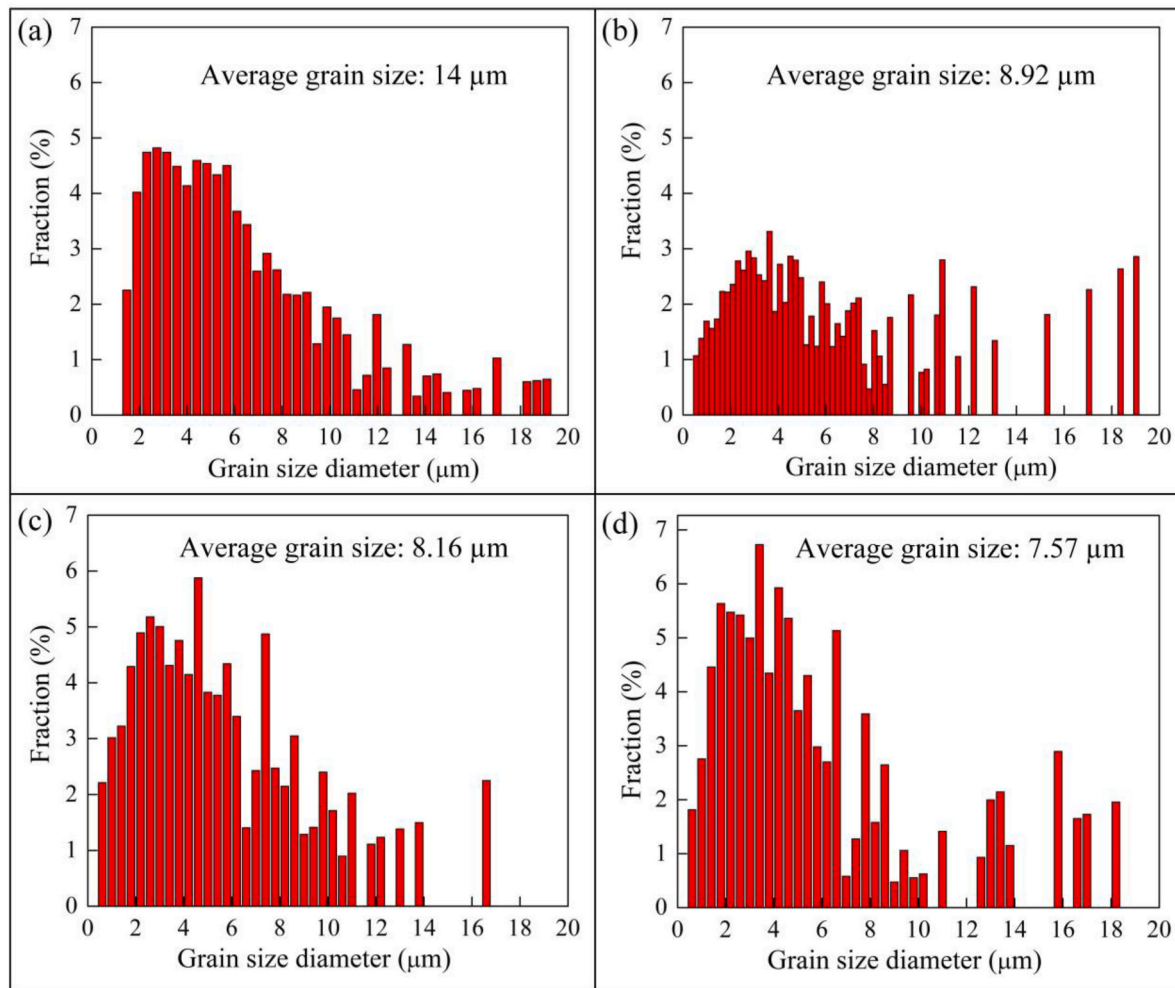
Fig. 17. Grain size statistical representation: (a) matrix average grain size, (b) average grain size for Exp no.1, (c) average grain size for Exp no.2, and (d) average grain size for Exp no.3.

Further microscopic analyses were conducted to understand any potential microstructural changes induced by machining, even if they're not instantly apparent in the XRD pattern. As shown in the SEM images in Fig. 16(a–c), the microstructure of the machined subsurface undergoes substantial plastic deformation. The grains were rotated and elongated in the cutting directions, indicating severe plastic deformation in the machined subsurfaces. Increased cutting parameters can transform the material's microstructure primarily due to intensified temperatures triggered by elevated friction during the machining process. Furthermore, the rapid heating and cooling cycles can also lead to amended material properties, including altered grain structures.

Moreover, the accelerated strain rates at higher machining input parameters can impact deformation mechanisms, influencing grain size, orientation, and texture within the material. As shown in the inverse pole figures, initially, at a lower cutting speed (i.e., Exp no.1), the grains were elongated along the cutting direction. This elongation occurs because the material experiences significant stress and strain in the cutting direction. However, with further increases in the cutting speed (i.e., Exp no. 2 and 3), the deformation causes the grains to break and reduce in size within the machined subsurface. The corresponding statistical data of grain refinement has been displayed in Fig. 17. As illustrated, the average grain size within the machined subsurface was 8.92, 8.16, and 7.57 μm for Exp no.1, 2, and 3, respectively. Moreover, when contrasted with the EBSD-derived average grain size of 14 μm for the Ti–6Al–4V matrix, it becomes evident that the machined subsurface grain size of the Ti–6Al–4V alloy undergoes refinement. The reduction in

grain size results from the intense shearing and deformation forces acting on the material during machining, leading to fragmentation and refinement of the grains within the surface layer of the workpiece [35].

The phase map (Fig. 16(g–i)) obtained through EBSD analysis indicated that the volume fraction of β-phase slightly decreased with increasing machining input parameters. For Exp no.1, the volume fraction of β-phase decreased from 7.5 % to 7.12 %. While for Exp no. 2 and 3, 6.95% and 6.63 % of the volume fraction of β-phase was retained, respectively. On the one hand, the decrease in the β-phase after rapid cooling supports the potential of cooling-induced phase changes. On the other hand, Rapid cooling can change the phase composition of material by favoring the production of the more stable phases from the metastable β-phase. Because of friction and distortion, the material experiences increased temperatures during machining. Following machining, fast cooling causes a quenching effect, forcing the material to harden quickly. This rapid cooling may limit the β-phase's stability, causing it to change into the α'-phase or other more stable phases at lower temperatures.

6. Conclusions

The present study implemented a thermo-metallo-mechanical coupled model that relied on phase transformation kinetics to anticipate and forecast phase transitions during the rapid heating and cooling stages in the context of HSM of Ti–6Al–4V. OM, SEM, EBSD, and XRD analyses were accomplished to recognize the accuracy of the developed

model. The following conclusions can be drawn based on the obtained results.

1. The developed model's chip geometrical features and cutting forces predictions aligned well with experimental data. The percentage relative error for chip geometrical parameters and cutting forces fell within the 5.15%–14.2% range. This suggests that the Ti–6Al–4V simulation model can accurately represent the stress-strain and temperature conditions during HSM and can provide a suitable framework for phase transformation analysis.

2. The simulation results showed that as the temperature at the chip's back surfaces for Exp nos. 1, 2, and 3 increased to 863.4, 972.4, and 1252 °C, respectively, the volume fraction of β-phase increased from 7.5% to 33.5, 63.56, and 96.89. Similarly, in the feed rate ranges from 0.15 mm/tooth to 0.25 mm/tooth (Exp nos. 4–6), the volume fraction of β-phase increased from 7.5% to 67.84%.

3. The predicted results also confirm that Exp nos. 1, 4, and 5 did not exhibit any phase transition at the tool-workpiece interface due to temperatures remaining considerably below the initial phase transformation temperature. However, for Exp nos. 2, 3, and 6, the volume percentage of the β-phase at the tool-workpiece interface increased from 7.5% to 20.53%, 30.14%, and 17.5%, respectively. In addition, all the experimental trials detected no phase transition at the machined surface.

4. During the rapid cooling phase, regions that experienced the β-phase during heating were converted back to α'-phases. Within the 150–350 m/min cutting speed range and feed rates of 0.15–0.25 mm/tooth, the volume fraction of α'-phases in the phase transformation regions increased to approximately 9.5%.

5. The XRD analysis indicated that no new peaks were obtained, confirming the absence of phase transformation on the machined surface. SEM and EBSD analyses revealed substantial plastic deformation in the machined subsurface. Elongated grains were observed at lower cutting speeds, but at higher cutting speeds, the deformation led to grain breakage and reduction in size within the machined subsurface.

Declaration of competing interest

Acknowledgment

References

[1] Sun W, Shan F, Zong N, Dong H, Jing T. A simulation and experiment study on phase transformations of Ti-6Al-4V in wire laser additive manufacturing. Mater Des 2021;207:109843. https://doi.org/10.1016/j.matdes.2021.109843.

[2] Ullah I, Zhang S, Zhang Q, Li BX. Microstructural and mechanical property investigation of machined surface layer in high-speed milling of Ti-6Al-4V alloy. Int J Adv Manuf Technol 2021;116:1707–19. https://doi.org/10.1007/s00170-021-07568-4.

[3] Che-Haron CH, Jawaid A. The effect of machining on surface integrity of titanium alloy Ti–6% Al–4% V. J Mater Process Technol 2005;166:188–92. https://doi.org/10.1016/j.jmatprotec.2004.08.012.

[4] Chen G, Ren C, Zhang P, Cui K, Li Y. Measurement and finite element simulation of micro-cutting temperatures of tool tip and workpiece. Int J Mach Tool Manufact 2013;75:16–26. https://doi.org/10.1016/j.ijmachtools.2013.08.005.

[5] Buffa G, Ducato A, Fratini L. FEM based prediction of phase transformations during Friction Stir Welding of Ti6Al4V titanium alloy. Mater Sci Eng, A 2013;581:56–65. https://doi.org/10.1016/j.msea.2013.06.009.

[6] Luo S, Yao J, Zou G, Li J, Jiang J, Yu F. Transformation characteristics of temperature and phases within Ti-6Al-4V aeroengine drum in hot forging and air cooling procedures. J Mater Res Technol 2020;9:8235–44. https://doi.org/10.1016/j.jmrt.2020.05.096.

[7] Ribamar GG, Mouráo dos Santos LP, Coelho HL, Jardini A, Gomes da Silva MJ, Gomes de Abreu HF, et al. Study of phase transformation in Ti-6Al-4V alloy produced by direct metal laser sintering. Proceedings of the 13th World Conference on Titanium 2016:1295–8. https://doi.org/10.1002/9781119296126.ch219.

[8] Bayoumi AE, Xie JQ. Some metallurgical aspects of chip formation in cutting Ti-6wt.%Al-4wt.%V alloy. Mater Sci Eng 1995;190:173–80. https://doi.org/10.1016/0921-5093(94)09595-N.

[9] Puerta Velásquez JD, Bolle B, Chevrier P, Geandier G, Tidu A. Metallurgical study on chips obtained by high speed machining of a Ti-6 wt.%Al-4 wt.%V alloy. Mater Sci Eng 2007;452–453:469–74. https://doi.org/10.1016/j.msea.2006.10.090.

[10] Wan ZP, Zhu YE, Liu HW, Tang Y. Microstructure evolution of adiabatic shear bands and mechanisms of saw-tooth chip formation in machining Ti6Al4V. Mater Sci Eng, A 2012;531:155–63. https://doi.org/10.1016/j.msea.2011.10.050.

[11] Wang Q, Liu Z, Yang D, Mohsan AUH. Metallurgical-based prediction of stress-temperature induced rapid heating and cooling phase transformations for high speed machining Ti-6Al-4V alloy. Mater Des 2017;119:208–18. https://doi.org/10.1016/j.matdes.2017.01.076.

[12] Zhang XP, Shivpuri R, Srivastava AK. Role of phase transformation in chip segmentation during high speed machining of dual phase titanium alloys. J Mater Process Technol 2014;214:3048–66. https://doi.org/10.1016/j.jmatprotec.2014.07.007.

[13] Ramesh A, Melkote SN. Modeling of white layer formation under thermally dominant conditions in orthogonal machining of hardened AISI 52100 steel. Int J Mach Tool Manufact 2008;48:402–14. https://doi.org/10.1016/j.ijmachtools.2007.09.007.

[14] Li B, Zhang S, Zhang Q, Chen J, Zhang J. Modelling of phase transformations induced by thermo-mechanical loads considering stress-strain effects in hard milling of AISI H13 steel. Int J Mech Sci 2018;149:241–53. https://doi.org/10.1016/j.ijmecsci.2018.10.010.

[15] Bailey NS, Katinas C, Shin YC. Laser direct deposition of AISI H13 tool steel powder with numerical modeling of solid phase transformation, hardness, and residual stresses. J Mater Process Technol 2017;247:223–33. https://doi.org/10.1016/j.jmatprotec.2017.04.020.

[16] Kaynak Y, Manchiraju S, Jawahir IS, Biermann D. Chip formation and phase transformation in orthogonal machining of NiTi shape memory alloy: microstructure-based modelling and experimental validation. CIRP Annals 2020;69:85–8. https://doi.org/10.1016/j.cirp.2020.04.025.

[17] Liu H, Xu X, Zhang J, Liu Z, He Y, Zhao W, et al. The state of the art for numerical simulations of the effect of the microstructure and its evolution in the metal-cutting processes. Int J Mach Tool Manufact 2022;177:103890. https://doi.org/10.1016/j.ijmachtools.2022.103890.

[18] Wang B, Liu Z, Cai Y, Luo X, Ma H, Song Q, et al. Advancements in material removal mechanism and surface integrity of high speed metal cutting: a review. Int J Mach Tool Manufact 2021;166:103744. https://doi.org/10.1016/j.ijmachtools.2021.103744.

[19] Avrami M. Kinetics of phase change. II Transformation-time relations for random distribution of nuclei. J Chem Phys 1940;8:212–24. https://doi.org/10.1063/1.1750631.

[20] Pan Z, Liang SY, Garmestani H, Shih DS. Prediction of machining-induced phase transformation and grain growth of Ti-6Al-4 V alloy. Int J Adv Manuf Technol 2016;87:859–66. https://doi.org/10.1007/s00170-016-8497-4.

[21] Ahmed T, Rack HJ. Phase transformations during cooling in $\alpha + \beta$ titanium alloys. Mater Sci Eng 1998;243:206–11. https://doi.org/10.1016/s0921-5093(97)00802-2.

[22] Liu Y, Mahmud A, Kursawe F, Nam TH. Effect of pseudoelastic cycling on the Clausius-Clapeyron relation for stress-induced martensitic transformation in NiTi. J Alloys Compd 2008;449:82–7. https://doi.org/10.1016/j.jallcom.2006.02.080.

[23] LaGrange T, Campbell GH, Turchi PEA, King WE. Rapid phase transformation kinetics on a nanoscale: studies of the $\alpha \rightarrow \beta$ transformation in pure, nanocrystalline Ti using the nanosecond dynamic transmission electron microscope. Acta Mater 2007;55:5211–24. https://doi.org/10.1016/j.actamat.2007.05.043.

[24] Deng D. FEM prediction of welding residual stress and distortion in carbon steel considering phase transformation effects. Mater Des 2009;30:359–66. https://doi.org/10.1016/j.matdes.2008.04.052.

[25] Malinov S, Guo Z, Sha W, Wilson A. Differential scanning calorimetry study and computer modeling of beta double right arrow alpha phase transformation in a Ti-6Al-4V alloy. Metall Mater Trans A 2001;32:879–87.

[26] Fan Y, Cheng P, Yao YL, Yang Z, Egland K. Effect of phase transformations on laser forming of Ti-6Al-4V alloy. J Appl Phys 2005;98. https://doi.org/10.1063/1.1944202.

[27] Liu D, Ni C, Wang Y, Zhu L, Zheng Z. Modified material constitutive model with activation energy for machining of selective laser melted Ti6Al4V alloys fabricated by different scanning strategies. J Mater Res Technol 2023;24:9612–29. https://doi.org/10.1016/j.jmrt.2023.05.125.

[28] Ullah I, Zhang S, Waqar S. Numerical and experimental investigation on thermo-mechanically induced residual stress in high-speed milling of Ti-6Al-4V alloy. J Manuf Process 2022;76:575–87. https://doi.org/10.1016/j.jmapro.2022.02.039.

[29] Wang C, Ding F, Tang D, Zheng L, Li S, Xie Y. Modeling and simulation of the high-speed milling of hardened steel SKD11 (62 HRC) based on SHPB technology. Int J Mach Tool Manufact 2016;108:13–26. https://doi.org/10.1016/j.ijmachtools.2016.05.005.

[30] Wang Q, Niu C, Liu Z, Wang Y, Cheng Y, Cui Y. The hardening effect of deformation twinning based on visco-plastic self consistent model and a multi-scale grain refinement prediction model during machining of titanium alloy. J Mater Res Technol 2023;26:1922–37. https://doi.org/10.1016/j.jmrt.2023.08.007.

[31] Li B, Zhang S, Hu R, Zhang X. Dislocation density and grain size evolution in hard machining of H13 steel: numerical and experimental investigation. J Mater Res Technol 2020;9:4241–54. https://doi.org/10.1016/j.jmrt.2020.02.051.

[32] Li BX, Zhang S, Zhang J. Plastic deformation and grain refinement in surface layer induced by thermo-mechanical loads for hard milling process. Proc IME B J Eng Manufact 2019;233:2033–46. https://doi.org/10.1177/0954405418815366.

[33] Liang X, Liu Z, Wang Q, Wang B, Ren X. Tool wear-induced microstructure evolution in localized deformation layer of machined Ti–6Al–4V. J Mater Sci 2020; 55:3636–51. https://doi.org/10.1007/s10853-019-04214-z.

[34] Vashista M, Paul S. Correlation between full width at half maximum (FWHM) of XRD peak with residual stress on ground surfaces. Phil Mag 2012;92:4194–204. https://doi.org/10.1080/14786435.2012.704429.

[35] Zhang Y, Bai Q. Microstructure effects on surface integrity in slot micro-milling multiphase titanium alloy Ti6Al4V. J Mater Res Technol 2023;25:6684–701. https://doi.org/10.1016/j.jmrt.2023.07.152.